

# Global Tropical Precipitation Relationships to Free-Tropospheric Water Vapor Using Radio Occultations

RAMON PADULLÉS,<sup>a,b</sup> YI-HUNG KUO,<sup>c</sup> J. DAVID NEELIN,<sup>c</sup> F. JOSEPH TURK,<sup>d</sup> CHI O. AO,<sup>d</sup> AND MANUEL DE LA TORRE JUÁREZ<sup>d</sup>

<sup>a</sup> *Institut de Ciències de l'Espai, Consejo Superior de Investigaciones Científicas, Barcelona, Spain*

<sup>b</sup> *Institut d'Estudis Espacials de Catalunya, Barcelona, Spain*

<sup>c</sup> *Department of Atmospheric and Oceanic Sciences, University of California, Los Angeles, Los Angeles, California*

<sup>d</sup> *Jet Propulsion Laboratory, California Institute of Technology, Pasadena, California*

(Manuscript received 23 February 2021, in final form 17 January 2022)

**ABSTRACT:** The transition to deep convection and associated precipitation is often studied in relationship to the associated column water vapor owing to the wide availability of these data from various ground or satellite-based products. Based on radiosonde and ground-based global navigation satellite system (GNSS) data examined at limited locations and model comparison studies, water vapor at different vertical levels is conjectured to have different relationships to convective intensity. Here, the relationship between precipitation and water vapor in different free-tropospheric layers is investigated using globally distributed GNSS radio occultation (RO) temperature and moisture profiles collocated with GPM IMERG precipitation across the tropical latitudes. A key feature of the RO measurement is its ability to directly sense in and near regions of heavy precipitation and clouds. Sharp pickups (i.e., sudden increases) of conditionally averaged precipitation as a function of water vapor in different tropospheric layers are noted for a variety of tropical ocean and land regions. The layer-integrated water vapor value at which this pickup occurs has a dependence on temperature that is more complex than constant RH, with larger subsaturation at warmer temperatures. These relationships of precipitation to its thermodynamic environment for different layers can provide a baseline for comparison with climate model simulations of the convective onset. Furthermore, vertical profiles before, during, and after convection are consistent with the hypothesis that the lower troposphere plays a causal role in the onset of convection, while the upper troposphere is moistened by detrainment from convection.

**KEYWORDS:** Convective storms; Thermodynamics; Occultation; Soundings


## 1. Introduction

The study of tropical convection and the resulting precipitation is motivated by difficulties in the representation of such features in general circulation models (GCM), and what this implies for the ability of current models to correctly simulate and project changes of precipitation (e.g., Sherwood et al. 2014). Analyses of TOGA COARE data have demonstrated that tropical deep convection is sensitive to free-tropospheric moisture (Brown and Zhang 1997; Parsons et al. 2000), consistent with subsequent modeling studies (Tompkins 2001; Derbyshire et al. 2004).

Bretherton et al. (2004) established a relationship between total column water vapor (TCWV; notation following GEWEX Data Assessment and Water Vapor Assessment Panels; e.g., Schröder et al. 2018) and precipitation with the Tropical Rainfall Measuring Mission (TRMM) observations. At short (subdaily) time scales, such a relationship can be understood as a transition to intense convection akin to a phase transition, with precipitation that picks up sharply when TCWV exceeds a critical threshold (Peters and Neelin 2006) that increases with bulk tropospheric temperature.

Analyses of tropical ARM site data have demonstrated that the observed precipitation–water vapor relation is consistent with lower free-tropospheric moisture impacting conditional instability through entrainment, and also noted upper-tropospheric moistening after precipitation (Holloway and Neelin 2009; Schiro et al. 2016). Offline plume buoyancy computations have suggested that the temperature dependence of the critical TCWV threshold seems to be a generic consequence of entrainment (Sahany et al. 2012). Further analyses quantified the relative contributions to conditional instability from different free-tropospheric layers versus boundary layer in terms of dynamic entrainment profiles (Ahmed and Neelin 2018; Schiro et al. 2018, 2020). These relationships provide a set of novel constraints on convective parameterizations (Kuo et al. 2018, 2020). They further suggest that moving beyond TCWV to information that can resolve contributions of different layers in the vertical is important to making these constraints more precise.

The relevant statistics characterizing the precipitation–water vapor relation (termed convective transition statistics) for tropical ocean basins and ARM site locations have been compiled using thermodynamic information from combinations of observational and reanalysis datasets (e.g., Neelin et al. 2009; Ahmed and Schumacher 2017). A source of uncertainty in many convective transition statistics is that the source of data for the global precipitation and the moisture typically comes from separate data products provided at different spatial or temporal scales, such as the Global Precipitation

 Denotes content that is immediately available upon publication as open access.

Corresponding author: Ramon Padullés, padulles@ice.cat

DOI: 10.1175/JAS-D-21-0052.1

© 2022 American Meteorological Society. For information regarding reuse of this content and general copyright information, consult the [AMS Copyright Policy \(www.ametsoc.org/PUBSReuseLicenses\)](#).

Measurement (GPM) Integrated Multi-satellitE Retrievals for GPM (IMERG) retrievals for precipitation, and moisture and temperature profiles from model reanalysis data. However, results relying on thermodynamic information from reanalyses can suffer from biases caused by the assimilation of radiances affected by rain (Padullés et al. 2018; Hersbach et al. 2015). Estimates of TCWV from passive microwave (MW) and infrared (IR) satellite observations [e.g., the TRMM Microwave Imager (TMI) and the Global Precipitation Measurement Imager (GMI)] often contain gaps in heavily precipitating regions that must be filled to restore missing information (Kuo et al. 2018). While a substantial fraction of the TCWV is located within the boundary layer, in this study the convective transition is assessed by the water vapor above the boundary layer. Estimation of lower layer moisture from passive MW sounders is challenging, owing to the high degree of overlap in the water vapor channel weighting functions used to invert the passive MW brightness temperatures, especially closer to the surface. Over land, interpretation of lower-free-tropospheric water vapor from passive MW brightness temperatures is dominated by the sensitivity to the high emissivity background surface. However, we acknowledge that the capability of extracting layer-averaged LFT moisture from passive MW or IR sounders has not been fully assessed. For example, there are some promising efforts to harness smallsat technologies for estimating near-surface specific humidity over ocean (e.g., the FluxSat concept; Gentemann et al. 2020).

To further study and constrain uncertainties in the precipitation–water vapor relation, in this work, we use the global navigation satellite systems (GNSS) radio occultation (RO) observations from the Constellation Observing System for Meteorology, Ionosphere and Climate (COSMIC)/FORMOSAT-3 (hereafter COSMIC) as the source of atmospheric thermodynamic properties. These include temperature, pressure, and water vapor pressure as a function of height. RO observations have been routinely acquired, processed, and assimilated into numerical weather prediction (NWP) for years (Healy et al. 2005; Cucurull et al. 2007), especially since the COSMIC constellation of six satellites dedicated to RO was launched in 2006 (Anthes et al. 2008). COSMIC has provided more than 7 million high-quality observations until early 2020, when the last satellite stopped providing data (Ho et al. 2020b). A new RO dedicated mission, COSMIC-2/FORMOSAT-7, was launched in 2019 to continue high-quality RO observations, focused on the tropical latitudes where the bulk of convective precipitation is situated (Schreiner et al. 2020; Ho et al. 2020a). For this study only COSMIC-1 data are used. However, the analysis could be further extended to COSMIC-2 era when the postprocessed data are made available (not yet at the time of writing).

RO has two major advantages over IR and microwave retrievals: 1) attenuation by clouds and precipitation at GNSS frequencies is insignificant compared with IR and microwave frequencies, making RO ideal for probing through deep-convective systems; 2) since it is a phase measurement, the RO retrieval algorithm does not require any radiance-level calibration and the GNSS data products are consistent among each other and independent of the source of precipitation data. Thus observations can be acquired regardless of surface type to provide global coverage.

RO observations are limited to some extent by their *along-track* coarse horizontal resolution (i.e., 100–200 km). Yet these scales are sufficient to infer robust relationships between water vapor and precipitation useful for GCM diagnostics (Kuo et al. 2020). In addition, the high quality retrievals (especially in free troposphere) with fine vertical resolution (~100 m to ~1 km depending on height) provided by RO allow us to infer these relationships within different vertical layers. These characteristics (global, all-weather coverage, vertical resolution) make RO data suitable for examining precipitation–water vapor relationships, permitting conjectures from limited radiosonde data to be assessed globally.

This manuscript is organized as follows: Section 2 describes the datasets used for this study. In section 3 we introduce the relationship between precipitation and the integrated column water vapor within different vertical layers of the troposphere for tropical regions. The dependence of these relationships with tropospheric temperature is discussed in section 4. In section 5, we examine the hypothesis that convection lifts moisture causing changes in vertical humidity distribution prior to and after precipitation and organized convective events. Finally, in section 6 we discuss the results and provide the conclusions.

## 2. Data

### a. Radio occultation data

The GNSS RO technique consists of a low-Earth-orbiting (LEO) satellite tracking the electromagnetic signals (L band, 1.575 GHz) transmitted from GNSS constellation satellites [e.g., the global positioning system (GPS) in the United States] while the satellite is occulting below Earth's horizon. This study uses COSMIC-1 data processed by the University Corporation for Atmospheric Research (UCAR), available from the UCAR COSMIC Data Archive Center (CDAAC) (UCAR COSMIC Program 2006).

As background, we briefly recap properties of this RO retrieval. The L-band signals bend due to the vertical gradient of the index of refraction ( $n$ ) as the radio link crosses deeper (and denser) atmospheric layers. Such vertical gradients can be inferred thanks to a very accurate tracking of the electromagnetic wave phase delays, which allows a precise knowledge of the bending angle suffered by the ray (Kursinski et al. 1997; Hajj et al. 2002). The bending angle is then transformed to a vertical profile of refractivity ( $N$ ), using an Abel integral (which assumes a spherical symmetry in the atmosphere), that can be related to thermodynamical parameters as (Thayer 1974; Kursinski et al. 1997)

$$N = (n - 1) \times 10^6 = 77.6 \frac{p}{T} + 3.73 \times 10^5 \frac{e}{T^2}, \quad (1)$$

where  $p$  is the total pressure (mb),  $T$  the temperature (K), and  $e$  the water vapor pressure (mb).

To obtain the thermodynamic parameters from observed  $N$ , additional constraints are needed. In the regions of the neutral (upper) atmosphere where water vapor can be neglected, hydrostatic equilibrium, the ideal gas law, and a boundary condition (e.g.,  $T$  at ~50 km) allow to solve for  $p$  and

*T*. However, when water vapor cannot be neglected, additional information is required. UCAR adopted a one-dimensional variational retrieval (IDVAR) in which *T*, *p*, and *e* are solved by obtaining the most probable combination in a statistically optimal way (Healy and Eyre 2000) starting with a priori information from the ERA-Interim (Dee et al. 2011). This implies that when there is little water vapor (e.g., higher layers), the retrievals are more sensitive to the temperature a priori, since its error results in larger fractional error in the water vapor. Similarly, the temperature in the lower layers is more sensitive to the water vapor a priori error. Departures from hydrostatic equilibrium could plausibly occur but this effect would be smaller than the uncertainty arising from the lack of spherical symmetry caused by the presence of horizontal gradients along the ray path, which is one of the known sources of errors for RO (Healy 2001).

The COSMIC RO observations provide global coverage and sample random local times since the satellites are positioned in different orbital planes. The vertical resolution of the observations ranges from 100 m near the surface to 1 km near the tropopause, and the horizontal resolution is considered to be between 100 and 300 km, although the major contribution to the bending angle comes from the region close to the tangent point (Anthes 2011), thus the effective horizontal resolution is actually higher.

In fact, each radio link is contributed by a tubular volume defined by the Fresnel cone in the cross-track direction and a Gaussian weighted contribution in the along-track direction centered at its tangent point. This results in a retrieved temperature accuracy below 0.5 K and a humidity accuracy of 10%–20% (Kursinski et al. 2000; Vergados et al. 2014). Comparisons between RO observations and radiosondes (e.g., de la Torre-Juárez and Nilsson 2003; Kuo et al. 2005; Sun et al. 2010; Wang et al. 2013; Vergados et al. 2014) have shown good agreement, i.e., RO provides soundings of radiosonde-comparable quality without the localization restriction. In comparison with other space-based sounders (infrared, microwave), RO outperforms them in terms of capability for sounding over land and over ocean, and regardless of cloud coverage.

We note that the collocation of RO, radiosonde, and high water vapor and precipitation conditions is limited, but the statistics evaluated here from RO–precipitation collocations can be compared to previous studies with radiosonde–precipitation collocations.

RO capabilities within the boundary layer depend on a number of factors. The most important ones are the loss of signals due to low signal to noise ratio, strong gradients (an effect called superrefraction) leading to problems in the refractivity inversion, and the atmospheric multipath effects that may lead to tracking errors (Ao et al. 2003; Sokolovskiy 2003). These result in a limited number of observations reaching heights below 1 km, and therefore, the number of observations is height dependent. The use of open loop tracking allows for better atmospheric penetration and enables the ability to also retrieve good quality rising occultations, dramatically increasing the total number of collected observations (Ao et al. 2009). Nevertheless, we assume that the RO profiles are usable at all heights wherever they are available,

provided they passed the quality control check performed by UCAR and provided along with the profiles (e.g., if a profile is truncated at 850 mb, the thermodynamic information is still valid for all the heights above this layer).

#### *b. IMERG surface precipitation data*

For precipitation we use the GPM IMERG V06B final run products (Huffman et al. 2019a), which provide gridded ( $0.1^\circ \times 0.1^\circ$ ) global surface instantaneous rain rates every 30 min. The period when data are available spans from June 2000 to the present. The precipitation rates are obtained from overpasses of passive microwave (PMW) sensors, intercalibrated to the GPM Combined Ku Radar-Radiometer Algorithm (CORRA) product, and completed with MW-calibrated IR derived precipitation. These are merged using a morphing Kalman filter (quasi-Lagrangian time interpolation scheme). It is finally scaled by precipitation gauges from the Global Precipitation Climatology Project (GPCP) when available (Huffman et al. 2019a,b). For the purposes of this study, these IMERG data will be averaged to a coarser  $1^\circ$  scale (see section 2d), which reduces the occurrences of false alarms and overall has better agreement with independent ground validation data (e.g., Tan et al. 2017). The main reason to choose the IMERG product over space-based radars is the high spatial and temporal coverage of the product, which maximizes the data collocation quantity. By contrast, the narrow swath of the space-based radars would dramatically reduce the number of collocations and therefore compromise the overall statistics. In terms of performance, several recent studies demonstrate the ability of IMERG V06 to represent well precipitation location and intensity, as well as the diurnal cycle (e.g., Tan et al. 2019a,b; Tang et al. 2020). This ensures that the statistical results over the long time span of the data used for the study should be reliable.

#### *c. Merged IR brightness temperature data*

To identify organized convective events, we use the NCEP/CPC L3 half-hourly 4-km global ( $60^\circ\text{S}$ – $60^\circ\text{N}$ ) merged IR product (Janowiak et al. 2017), which provides snapshots of 4-km-pixel-resolution  $10.8\text{-}\mu\text{m}$  IR brightness temperature ( $T_{B11}$ ) every 30 min merged from geostationary satellites. For each IR snapshot, we identify mesoscale convective systems (MCS) following the Mohr and Zipser (1996) criterion: an area with  $T_{B11}$  below 250 K of at least 2000 km<sup>2</sup>, and with an enclosed minimum  $T_{B11}$  below 225 K. This is very similar to several related methods (Houze 1993; Nesbitt et al. 2006; Vila et al. 2008; Yuan and Houze 2010; Fiolleau and Roca 2013), each using this channel of IR brightness temperature and similar thresholds. Some MCS definitions augment this duration or propagation information (e.g., Chen et al. 2019; Núñez Ocasio et al. 2020) or with additional information from precipitation radar or microwave (Yuan and Houze 2010; Feng et al. 2018, 2019, 2021). We use the standard IR-based criterion because it provides information over much wider range of spatial and temporal points, and avoids any concern that the criterion might directly affect the precipitation statistics when comparing between MCS cases versus non-MCS cases (as might occur for MCS identification methods that also include precipitation criteria). After MCS features are identified

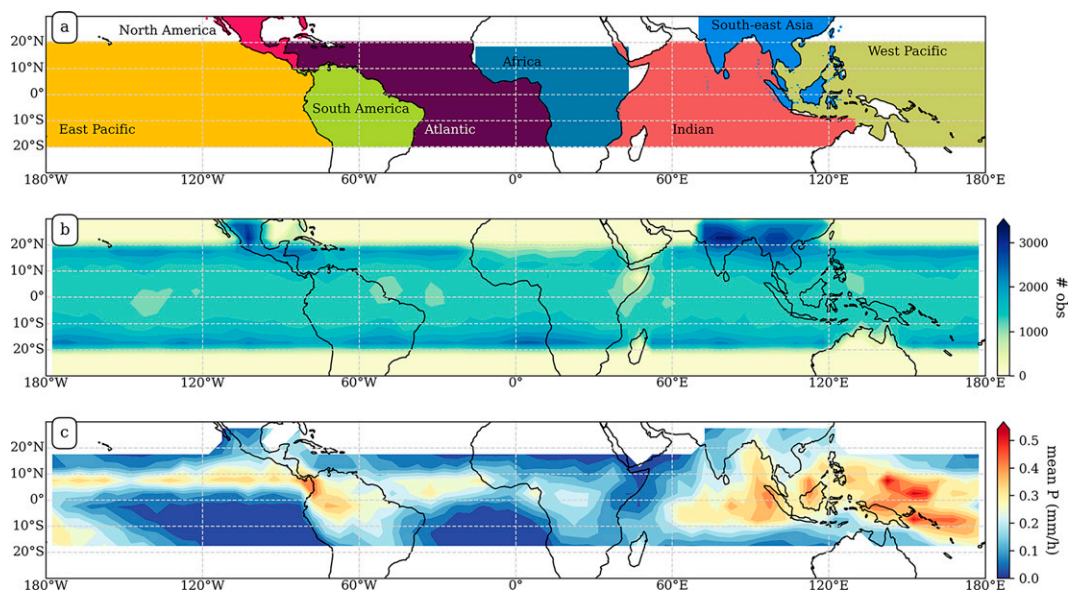


FIG. 1. (a) Identification of the regions employed in the analysis to separate the data into different land and oceanic regions, separated by different colors and labeled accordingly. (b) Two-dimensional histogram indicating the number of RO observations from the COSMIC-1 mission on a grid of  $5^\circ \times 5^\circ$  used in the analysis. (c) Mean value of the collocated precipitation rain rate on the same grid of  $5^\circ \times 5^\circ$  as in (b).

for each snapshot, for each geographical location at a given time, we can determine whether it is inside an MCS, or the time (within a 12-h window) before MCS arrival or after that location was last within an MCS.

#### d. Colocations

Vertical profiles of thermodynamic parameters provided by RO are associated with a representative location of the sampled region. Such location is called the occultation point, and in the case of the retrievals from UCAR, it is defined as the projection on the surface of the location of the tangent point of the ray whose height is approximately 3–4 km. The precipitation linked to each RO sounding is the average of the IMERG precipitation in an area of  $1^\circ \times 1^\circ$  centered at the occultation point. The IMERG file used to obtain the precipitation rates is the one corresponding to the nearest 30 min snapshot from the occultation time. The precipitation spatial pattern might evolve during this time interval, the effect of which is somewhat mitigated by the large  $1^\circ$  spatial averaging (e.g., Tan et al. 2017). The MCS status is derived by inspecting the area of merged IR brightness temperatures centered at the occultation point, similar to what is done with IMERG.

In addition to the precipitation and IR brightness temperatures at the RO observation time, we also store the values of precipitation and brightness temperatures around the occultation point corresponding to the  $\pm 6$  h with respect to the observation time. Therefore, we have the time evolution of the precipitation and IR brightness temperatures at such location for a 12-h window and every 30 min.

Such collocations are performed for almost the whole COSMIC-1 mission. The coincidences are only obtained over

the tropics (i.e.,  $\pm 25^\circ$  of latitude, reaching  $\pm 30^\circ$  for certain land areas; see Fig. 1). This results in data starting from April 2006 to December 2017 (after which the COSMIC-1 data started to decrease dramatically), including  $\sim 2.1$  million soundings. Figure 1 shows the general statistics of the collocated observations. Figure 1a indicates the different regions used to separate the data into different land and oceanic basins. Figure 1b shows a two-dimensional histogram indicating the number of RO observations used for every  $5^\circ \times 5^\circ$  grid cell. And Fig. 1c shows the mean precipitation rain rates for collocated observations in the same  $5^\circ \times 5^\circ$  grid cells as Fig. 1b.

### 3. Precipitation transition statistics derived from RO

The global distribution of RO observations and their vertical resolution allow us to explore the relationships between the layer-integrated water vapor between different pressure layers with precipitation, for different oceanic and land regions. The layer-integrated water vapor between two pressure layers is defined as

$$\text{layer wv} = \int_{p_i}^{p_f} w(p) dp/g, \quad (2)$$

where  $w$  is the mixing ratio,  $p$  is the pressure, and  $g$  is the gravitational acceleration. Figure 2 shows such relationships for the oceanic basins, and in Fig. 3 for different land regions. In these plots, the precipitation is conditionally averaged on the layer-integrated water vapor between the indicated pressure levels. This is done for data corresponding to different tropospheric average temperature  $\bar{T}$ :



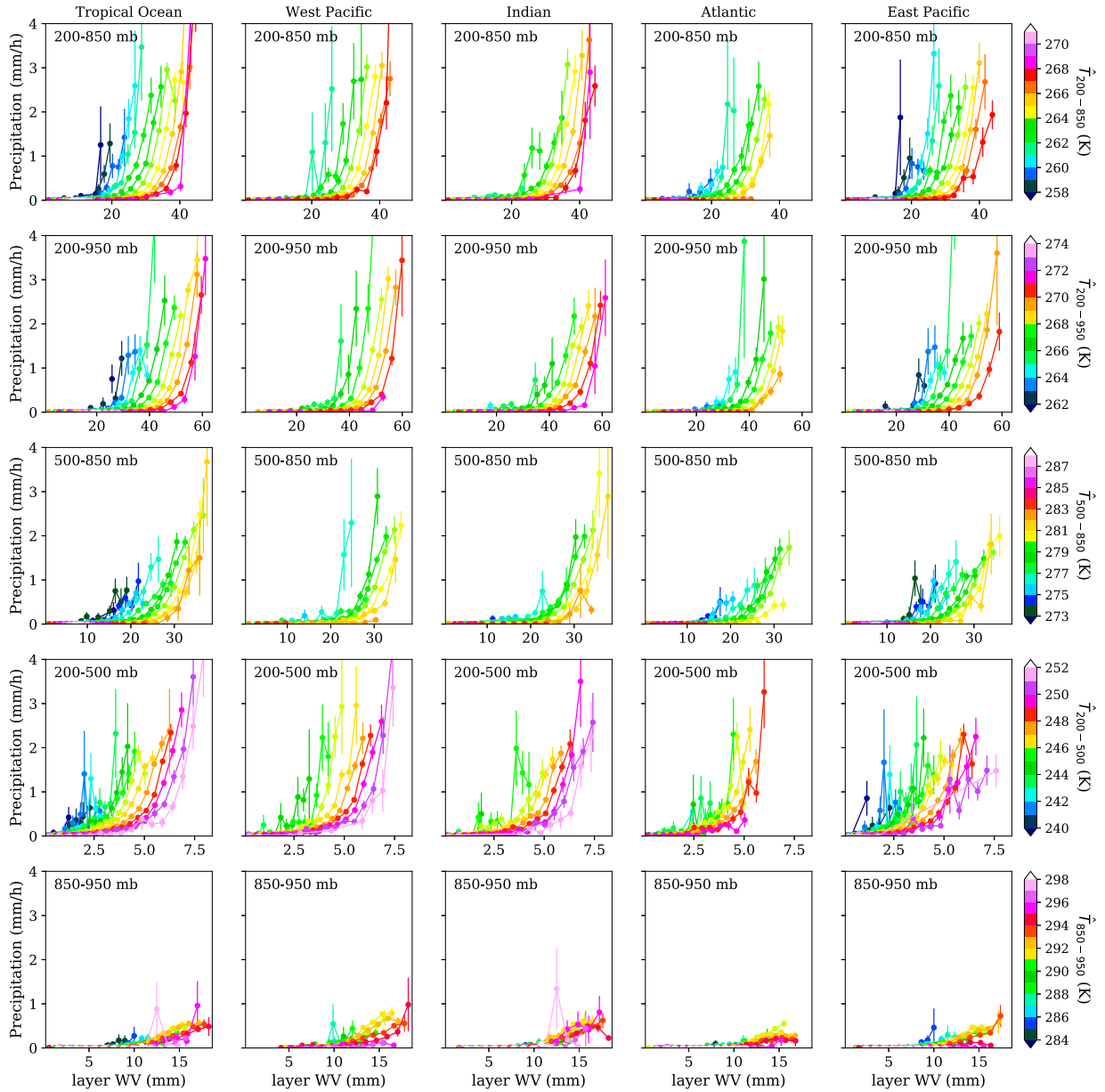


FIG. 2. Relationship between precipitation and layer-integrated water vapor for different ocean basin regions and different vertical layers of the atmosphere. Error bars indicate the standard error. Different rows correspond to different layers, and the different columns relate to different regions. The regions are (from left to right) all tropical ocean regions, the west Pacific, Indian Ocean, Atlantic, and the east Pacific. The layers are (from top to bottom) the free troposphere (200–850 mb), from 200 to 950 mb, from 500 to 850 mb, from 200 to 500 mb, and from 850 to 950 mb. The color bar indicates the mean temperature between the same pressure levels indicated for the rows.

$$\hat{T} = \frac{\int_{p_i}^{p_f} T(p) dp / g}{\int_{p_i}^{p_f} dp / g}, \quad (3)$$

averaged between the same pressure levels as the water vapor, indicated by the different colors (linked to color bar in the right side of each row). The temperature bins correspond to 1 K. The bins of layer-integrated water vapor are defined depending on

each situation, representing approximately 16 regular bins covering the whole range of water vapor in each tropospheric layer (resulting in, e.g., ~3 mm between 200 and 850 mb, and ~0.4 mm in the 200–500-mb interval). We identify the free troposphere as the 200–850-mb layer. Within the free troposphere, the simplest split is between the lower free troposphere (LFT; 500–850 mb) and the upper free troposphere (UFT; 200–500 mb). This choice is also motivated by evidence that inflow into convective updrafts through the lower-free-tropospheric layer causes substantial

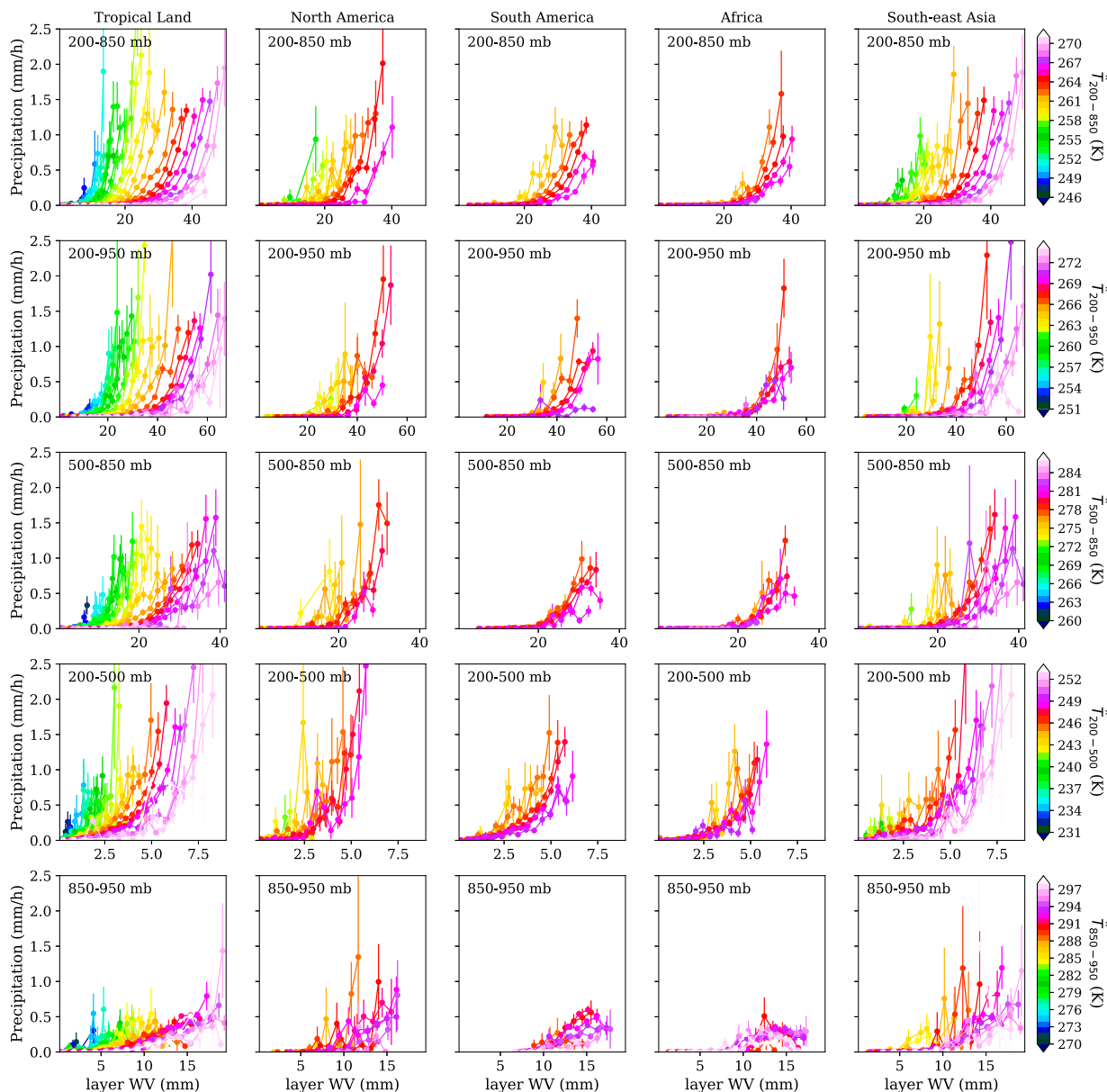


FIG. 3. As in Fig. 2, but for the cases over land regions. The different columns correspond to the summary for (from left to right) all land cases, North America, South America, Africa, and Southeast Asia. The different rows and the color bars are as in Fig. 2.

influence of environmental water vapor on convection (e.g., Zipser 1977; Kingsmill and Houze 1999; Mechem et al. 2002; Ahmed and Neelin 2018; Schiro et al. 2018). The 850 mb boundary is chosen to minimize influence of boundary layer turbulence on the free-tropospheric layer. The 850–950-mb layer is an imperfect match to the boundary layer, limited by the number of low-level retrievals, but is strongly connected to boundary layer properties. We thus refer to this for brevity as the boundary layer, and include statistics based on water vapor in this layer for reference compared to the free-tropospheric layers of focus. Missing boundary layer profiles are likely to be more frequent in

regions of inversions (Ao 2007), but we are not aware of any effect that would bias sampling within the deep convective regions with respect to, e.g., deep convective life cycle.

The first column in each of Figs. 2 and 3 shows the global tropical ocean and land, while the rest of the columns show the results for the different regions. The regions are the west Pacific, the Indian Ocean, the Atlantic, and the east Pacific, for the ocean regions, and North America, South America, Africa, and Southeast Asia for the tropical land regions. Such regions are shown in Fig. 1 with different colors.

Overall, there exists a sharp “pickup” (i.e., a sudden increase) of the precipitation after a critical value of layer-integrated

water vapor, that depends on the  $\widehat{T}$ , for most pressure levels and both over ocean and land. However, different behaviors and subtle differences are worth noting. First of all, it is important to emphasize the obvious difference in the pickups using pressure levels contained in the so-called free troposphere (e.g., above 850 mb) and within the boundary layer (i.e., the bottom row for both ocean and land, comprising the pressure levels between 850 and 950 mb). The pickup using the boundary layer water vapor (Figs. 2 and 3, fifth row) is less sharp than using the free-tropospheric water vapor, especially over ocean. Over land, this relationship is also less obvious, although it captures the stronger effect of the boundary layer than over ocean. This difference between the relationships using the boundary layer and the free troposphere is in agreement with relationships at localized ARM sites (Holloway and Neelin 2009; Schiro and Neelin 2019), confirming the importance of free-tropospheric water vapor in the onset of deep convection throughout the tropics.

Within the free troposphere, there is a difference between the precipitation–layer-integrated water vapor relationship in the LFT and UFT. The pickup is less sharp in the UFT: the precipitation starts increasing smoothly with water vapor, instead of sharply increasing after a critical value of water vapor. This difference between the UFT and LFT is further investigated in sections 4 and 5. The clearer threshold hints at a stronger causality relationship between the LFT water vapor and the onset of deep convection, while the relationship with the UFT water vapor is more complicated. The interpretation of causality relationships is nontrivial because water vapor can both affect conditional instability driving deep convection and be changed by the convection. A leading pathway by which lower-tropospheric humidity values have a causal influence is through entrainment (Holloway and Neelin 2009; Kuo et al. 2017). Note that this does not imply that LFT humidity is a sole cause of deep convection but that it can be important factor in affecting it—along with other factors such as convective inhibition (CIN; Mapes 2000; Elsaesser and Kummerow 2013). These relationships are further discussed in section 5.

Regional differences may be noted. Over ocean regions, one of the main differences is the observed temperature range: the Atlantic reaches the lowest  $\widehat{T}$ , largely associated with the slightly cooler climatology in the Atlantic. The Indian Ocean and the west Pacific exhibit similar features, while the east Pacific is the region with the largest temperature range. The pickup curves tend to behave similarly for a given temperature, although noting that the Atlantic and east Pacific tend not to reach conditional-average precipitation values as high as those in the Indian and west Pacific.

Over land, similar overall conclusions stand as over ocean, although some aspects of the relationships are less clear-cut. Several factors may contribute to this. First, over land the influence of the boundary layer is expected to be stronger. Relationships between the free-tropospheric water vapor and precipitation lack the component from the layers below and therefore become less sharp. The 850–950-mb layer captures some of the larger boundary layer contribution (bottom row of panels in Fig. 3), but is far from a perfect measure since the near-surface portion is missing. Second, there are fewer data

points over land, because ocean areas are larger, and the number of profiles over land is also limited by topography features. Third, the precipitation information comes from MW and IR observations and land surface emissivity may also affect the quality (as mentioned above). In regional differences, the region abbreviated as Southeast Asia has the widest range of temperatures simply because of its broad latitudinal span. Over Africa, the separation of the curves with temperature is less obvious than for other regions. We note caveats on the African region in terms of in situ information available to inform precipitation retrievals and the reanalysis first guess for the COSMIC retrievals. However, the RO temperature and moisture retrievals have the same basis as other regions, and there is reasonable sampling of heavy rain occurrences in this region.

#### 4. Dependence of the pickup curves on temperature

From Figs. 2 and 3 it seems clear that the pickup behavior of precipitation with layer-integrated water vapor depends on the temperature. Moreover, what depends on temperature is the critical value of layer-integrated water vapor where precipitation sharply increases (e.g., Neelin et al. 2009). For every different pressure ranges and regions in Figs. 2 and 3, we look for the critical value of layer water vapor,  $\text{LWV}_{\text{crit}}$ , where precipitation sharply increases. To do so, we take as a reference the precipitation–layer-integrated water vapor curve containing the largest number of points (at each different panel, i.e., the  $\widehat{T}$  bin containing more points) and we identify its  $\text{LWV}_{\text{crit}}$  where it crosses the precipitation = 0.4 mm h<sup>-1</sup>. This value is chosen to give a value near the start of the rapid pickup that works for a wide range of curves, and to resemble the fits used in Neelin et al. (2009). Similar to Kuo et al. (2018), the pickup curves for other values of  $\widehat{T}$  are then shifted to best fit this reference curve, with the shifts giving  $\text{LWV}_{\text{crit}}$  relative to that of the reference curve.

Figure 4 shows the relationship between precipitation and the layer-integrated water vapor scaled by its critical value for the pressure levels between 200 and 850 mb, i.e., the whole free troposphere. The extent to which the curves corresponding to every  $\widehat{T}$  collapse tests how well the critical value alone is sufficient to describe the temperature dependence. In Fig. 4a we see how the curves for all oceanic regions nicely collapse, showing a sharp increase of precipitation around the critical value, as in previous studies (Peters and Neelin 2006; Neelin et al. 2009; Sahany et al. 2012; Kuo et al. 2018). The collapse is also visible for the land regions (Fig. 4c), although in this case, some spread appears. As we mentioned in the previous section, over land the influence of the boundary layer and the surface is expected to play a more important role than over ocean (e.g., Ahmed and Schumacher 2017); therefore, such behavior is expected. To simplify the visualization of the collapsed curves in Figs. 4a, 4c, 5a, 5c, 6a, and 6c, the different points have been drawn using different symbols depending on the standard error of each measurement. Closed circles show the measurements with a standard error lower than 0.15 mm h<sup>-1</sup>, open circles represent the data with a standard error between 0.15 and 1.5 mm h<sup>-1</sup>, and the small dots show the data with a standard error larger than 1.5 mm h<sup>-1</sup>. Large standard errors in these data are associated with underpopulated bins.

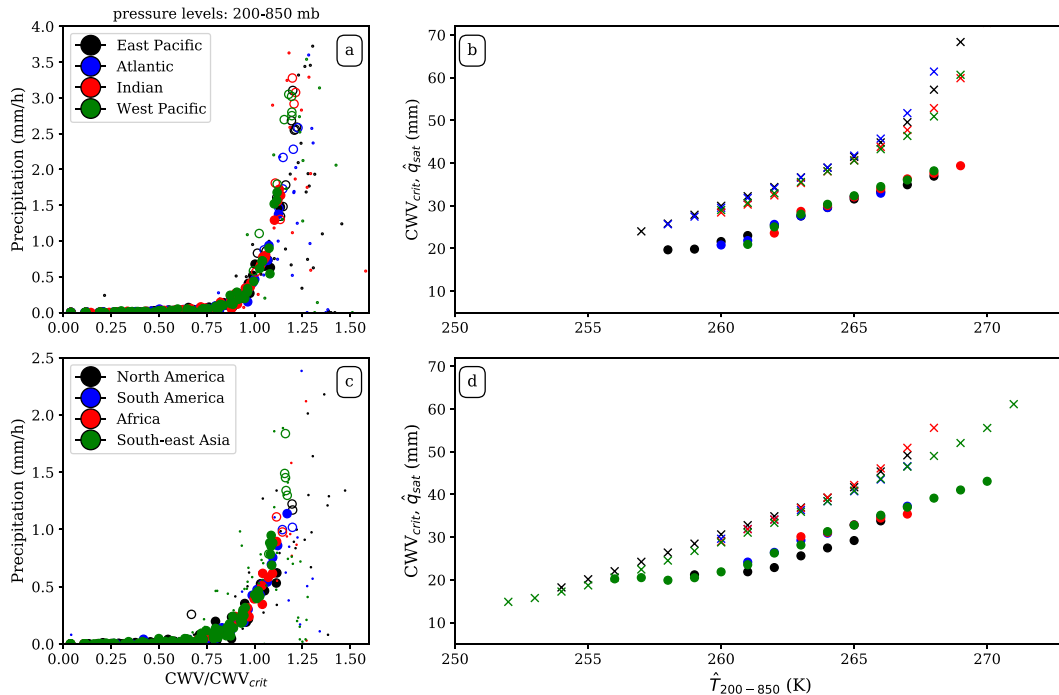


FIG. 4. Collapse of the curves for all  $\hat{T}$  for the 200–850-mb pressure range: (a) Precipitation as a function of the layer-integrated water vapor rescaled by the critical value corresponding to each  $\hat{T}$  for the ocean cases. (b) Critical layer-integrated water vapor (circles) and  $\widehat{q}_{\text{sat}}$  (crosses) as a function of  $\hat{T}$  for the ocean cases. (c) As in (a), but for land cases. (d) As in (b), but for land cases. The closed circles [in (a) and (c)] represent measurements with standard error lower than  $0.15 \text{ mm h}^{-1}$ ; the open circles identify measurements with standard error larger than  $0.15 \text{ mm h}^{-1}$  and lower than  $1.5 \text{ mm h}^{-1}$ ; the small dots indicate measurements with standard error larger than  $1.5 \text{ mm h}^{-1}$ , associated with underpopulated bins in this dataset.

The circles in Figs. 4b and 4d show the dependence of  $\text{LWV}_{\text{crit}}$  with  $\hat{T}$ . The critical value  $\text{LWV}_{\text{crit}}$  increases approximately linearly with  $\hat{T}$ , for all regions and for all the  $\hat{T}$  range. Furthermore, the values for different regions agree well. The saturation value integrated along the corresponding pressure layers,  $\widehat{q}_{\text{sat}} = \int_{p_i}^{p_f} q_{\text{sat}} dp/g$ , is also shown (represented as crosses in the right panels). For this pressure range (200–850 mb), the  $\text{LWV}_{\text{crit}}$  represents roughly a constant fraction of the  $\widehat{q}_{\text{sat}}$  for  $\hat{T}$  between 262 and 265 K. However, above 265 K,  $\text{LWV}_{\text{crit}}$  does not increase as quickly as  $\widehat{q}_{\text{sat}}$ . This implies that the subsaturation, i.e., the LWV interval between  $\text{LWV}_{\text{crit}}$  and saturation ( $\widehat{q}_{\text{sat}}$ ) increases with temperature.

Figures 5a and 5c show the collapse of the pickup curves for the pressure levels between 500 and 850 mb. The collapse is clear for the tropical ocean regions, whereas some spread appears for the tropical land cases. Such spread is mainly contributed by the points obtained from smaller data samples, and specific regions like North America. The larger spread in the collapse of the curves for all  $\hat{T}$  over land is also seen in the behavior of the  $\text{LWV}_{\text{crit}}$  as a function of  $\hat{T}$  (Fig. 5d), where the increase with temperature shows more variation among regions than over ocean (Fig. 5b). Compared to the 200–850-mb pressure range, the increase of subsaturation with temperature is

more substantial over both ocean and land. For Africa, this is particularly noticeable, with  $\text{LWV}_{\text{crit}}$  roughly similar for high and low temperatures.

Comparing these results with the ones for the upper troposphere (200–500 mb), shown in Fig. 6, it can be seen that for this pressure range the collapse is less sharp for both ocean and land. This was already noticed in Figs. 2 and 3, where the increase of precipitation with layer-integrated water vapor starts at lower values and is smoother (i.e., spread over a larger range of water vapor) than for the 200–850- and 500–850-mb pressure ranges. However,  $\text{LWV}_{\text{crit}}$  increases approximately linearly with  $\hat{T}$  as in the other pressure ranges.

The relative sharpness of the collapsed curves can be examined for consistency with causality relationships postulated in previous studies. The heaviest precipitation appears once the layer-integrated water vapor exceeds a certain  $\text{LWV}_{\text{crit}}$  that depends on temperature but is significantly subsaturated. This  $\text{LWV}_{\text{crit}}$  has been postulated to be associated with the onset of deep convection through conditional instability, with entrainment in the LFT creating a strong dependence on moisture in that layer (Holloway and Neelin 2010; Kuo et al. 2017). Over ocean, the moisture dependence is a leading effect, while over land, boundary layer variations also play a significant role (Schiro et al. 2018; Ahmed and Neelin 2019). In the UFT detrainment and consequent moistening by deep convection is



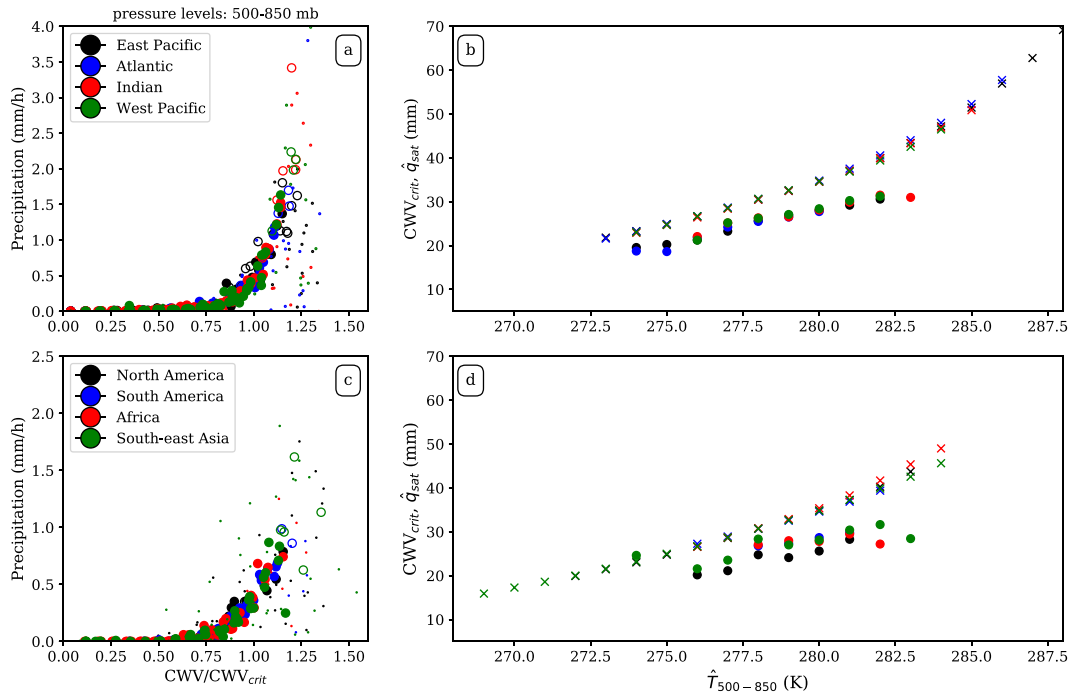


FIG. 5. Collapse of the curves for all  $\hat{T}$  as in Fig. 4, but for the 500–850-mb pressure range.

postulated to dominate (Del Genio et al. 2012; Schiro et al. 2016; Brenowitz and Bretherton 2018). Based on this, the observation that the LFT water vapor seems to have a stronger relationship with precipitation and exhibits a sharper pickup than in the UFT hints at consistency with the postulated causal

role for LFT water vapor. Likewise, the smaller scatter in the 850–500-mb layer-integrated water vapor relationship over ocean than over land appears consistent with the smaller role of oceanic boundary layer environmental humidity variations in impacting conditional instability relative to LFT impacts. Here,

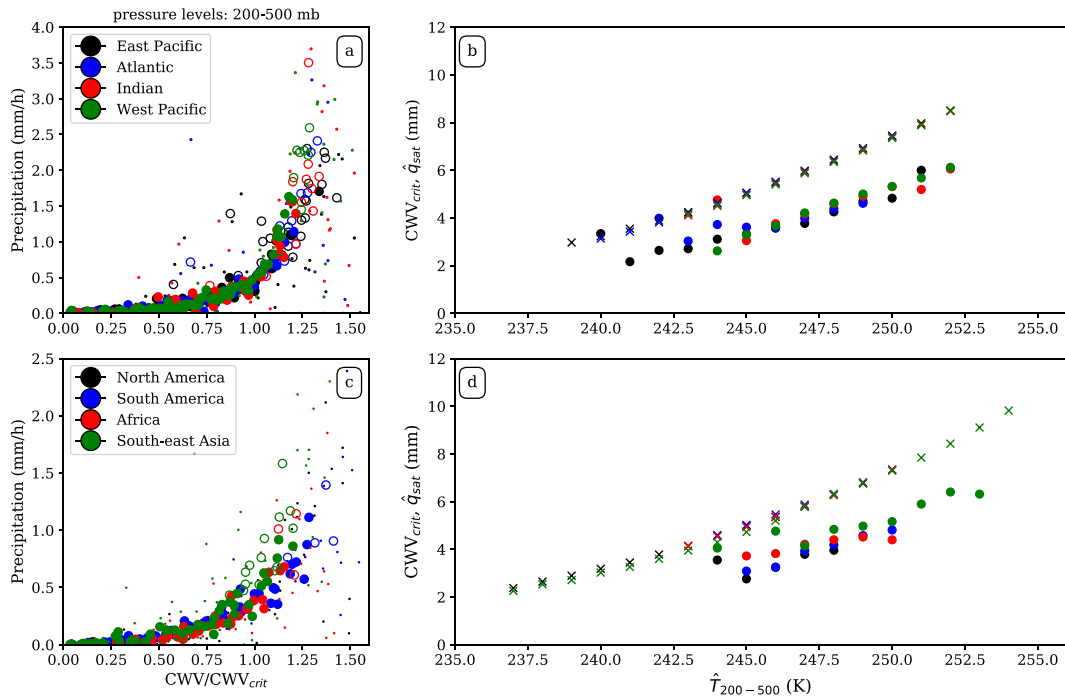


FIG. 6. Collapse of the curves for all  $\hat{T}$  as in Fig. 4, but for the 200–500-mb pressure range.

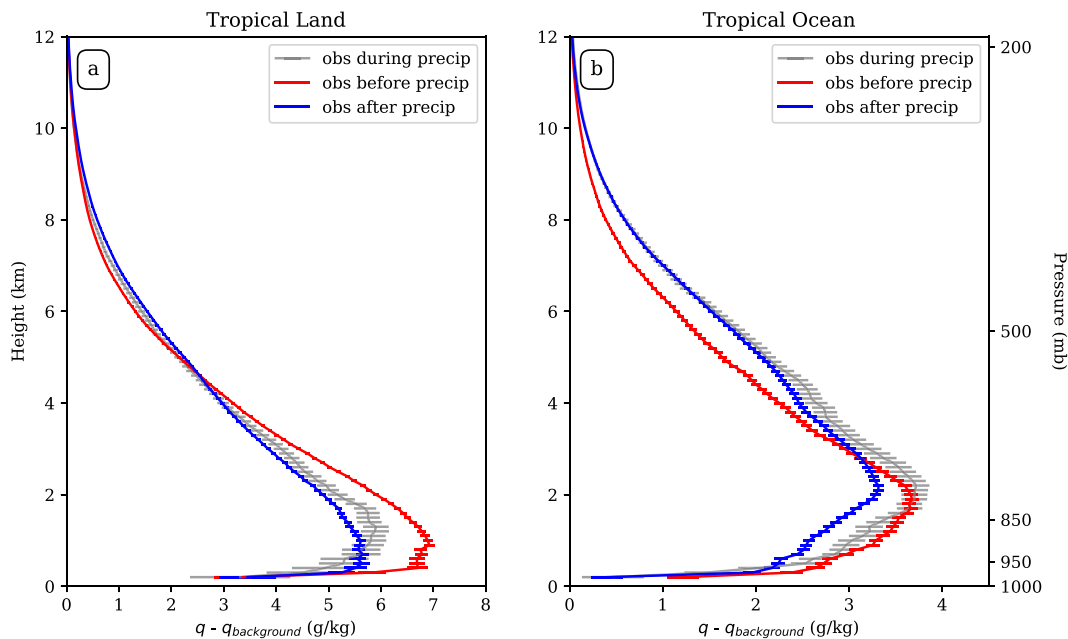


FIG. 7. Mean specific humidity vertical profile for the cases where the observation happens during precipitation (gray), before precipitation (red), and after precipitation (blue) with respect to a mean specific humidity background profile obtained with no precipitation (in the  $\pm 6$  h of the observation) for (left) land cases and (right) ocean cases as a function of height. The solid line represents the mean, while the horizontal lines represent the standard error. For comparison purposes, a reference pressure level is shown in the right axis.

environmental humidity variations refers to those at scales observed by the RO retrievals, i.e., larger than the typical scale of deep convective elements. Boundary layer variations at scales close to that of the deep convection can potentially be important for convective initiation (Li and Carbone 2012). To provide further evidence for such causal relationships is the aim of the next section.

## 5. Changes in moisture profile with respect to convection

To further investigate the causal relationships between convective onset and moisture in different tropospheric layers, we study the time evolution of specific and relative humidity vertical profiles with respect to convection. Radiosonde based studies at limited locations (Holloway and Neelin 2009; Schiro et al. 2016) have indicated that lower-tropospheric water vapor must be high preceding convection due to its effects on buoyancy. These studies also noted that upper-tropospheric water vapor tends to be higher after convection, consistent with lofting in updrafts, detrainment, and evaporation of condensate. With RO measurements, we can examine this over the global tropics. By combining with information from geostationary satellites and IMERG, we can examine changes in vertical moisture structure preceding, during, and after all precipitation events or MCS events.

### a. Moisture profile before/after precipitation

We first group all the observations into three categories: those obtained after precipitation ( $P > 0.6$  mm h<sup>-1</sup> before the

observation;  $P = 0$  mm h<sup>-1</sup> after the observation), those obtained during precipitation ( $P > 0.6$  mm h<sup>-1</sup> in the time range comprising half and hour before and half an hour after the observation), and those obtained before precipitation ( $P > 0.6$  mm h<sup>-1</sup> after the observation;  $P = 0$  before the observation). For each group, the mean specific humidity ( $q$ ) and RH are computed, together with the corresponding standard error. Figure 7 shows the  $q$  anomaly for the three groups with respect to a  $q_{\text{background}}$  obtained when there is no rain in the  $\pm 6$  h of the observation, over tropical ocean (Fig. 7a) and over tropical land (Fig. 7b). Figure 8 shows the mean RH for the three groups, over tropical ocean (Fig. 8a) and over tropical land (Fig. 8b). As expected, the typical environment profile associated with deep convection is substantially below saturation, since the convection arises by conditional instability, rather than by large-scale saturation of the environment.

Focusing on Fig. 7, the first relevant feature we observe is that there is a substantial increase of moisture in the precipitating cases with respect to the nonprecipitating ones (i.e., background), for all temporal situations and for all the vertical layers. Such increase, while it is comparable between over ocean and over land in the upper and middle free troposphere, is larger over land in the bottom layers of the troposphere. This can be explained by the stronger influence of the surface and boundary layer over land than over ocean, and therefore, a larger difference between precipitating and nonprecipitating scenarios is observed in these layers. Over ocean, the largest difference in moisture between precipitating and nonprecipitating scenarios happens in the lower free troposphere.

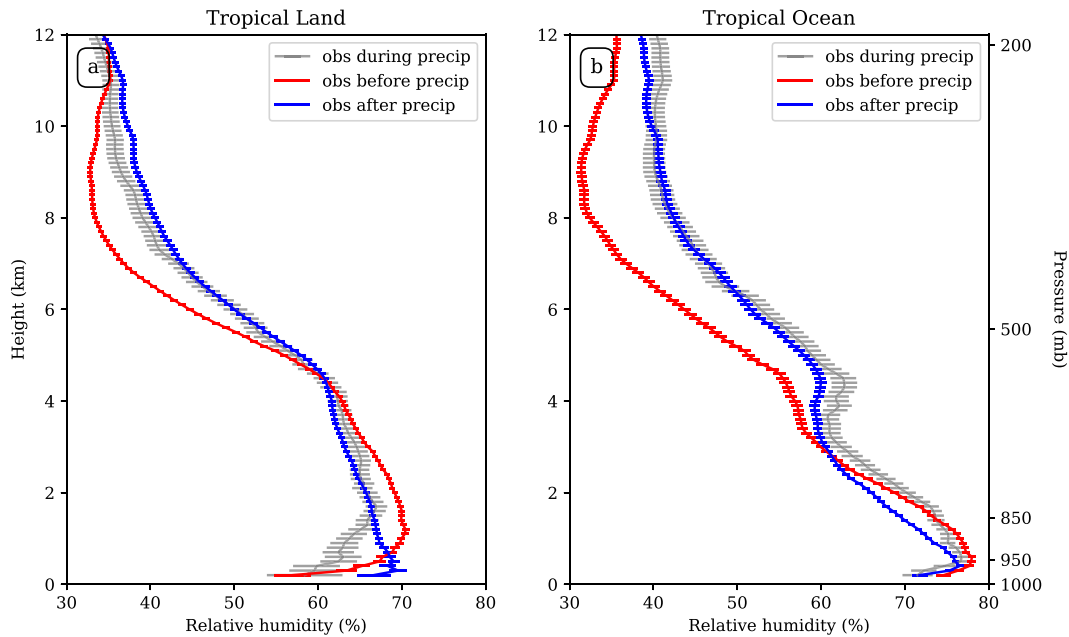


FIG. 8. Mean RH vertical profile for the cases where the observation happens during precipitation (gray), before precipitation (red), and after precipitation (blue) for (left) land cases and (right) ocean cases as a function of height. The solid line represents the mean, while the horizontal lines represent the standard error. For comparison purposes, a reference pressure level is shown in the right axis.

Once we look at the different times of observation with respect to precipitation, the more obvious thing is that the upper free troposphere is substantially wetter after rain than before rain, especially over ocean. Therefore, one can confirm the hypothesis that the upper free troposphere is partially moistened by precipitation, instead of playing a key role in initiating precipitation.

On the other hand, the large increase of moisture in the lower free troposphere before precipitation points toward the causal relationship that these layers may have on the onset of deep convection. These features, specially above 900 mb, are consistent with the results in Schiro et al. (2016).

Figure 8 shows the mean RH profiles for the three different temporal scenarios with respect to precipitation. We can see how the RH in the middle and upper free troposphere is larger after precipitation, and that the RH is larger before and during precipitation in the lower layers, supporting the same hypothesis as in the previous paragraphs. Therefore, results in Fig. 8 are consistent with those in Fig. 7.

Quantifying the difference between the mean  $q$  anomaly before and after precipitation, the increase in the UFT of the profile corresponding to after precipitation with respect to before is about 20% over land and 25% over ocean. The increase in the LFT of the profiles corresponding to before precipitation with respect to after precipitation reaches 10% over land, while it reaches 5% over ocean. In the case of the relative humidity, the relative difference between the mean RH profiles after precipitation with respect to before precipitation in the UFT reaches 18% over land and 22% over ocean. In the LFT, the relative difference between the before

and the after precipitation reaches around 6% both over ocean and over land.

b. Moisture profile before/after MCS

Mesoscale convective systems exhibit complex structures, with some precipitation-free regions under thick stratiform cloud cover, and with localized updrafts affecting other parts of the system. Complementary to the approach in the previous subsection, we present the time evolution of moisture profiles with respect to organized systems [for precipitation–water vapor relationship conditioned on MCS, see Schiro et al. (2020)].

Figure 9 shows the mean specific and relative humidity profiles over tropical land and ocean similar to Figs. 7 and 8, but before, during, and after MCS. In the upper troposphere, Figs. 9c and 9d show RH much higher than in Fig. 8, consistent with the MCS criterion based on low brightness temperature (indicating higher cloud top). Many of the features noted earlier in Figs. 7 and 8 are still valid. For example, specific humidity is significantly higher than background in the vicinity of MCS (up to 6 h before and after). Also, there is a greater difference in the boundary layer over land than ocean (Fig. 9a), suggesting importance of boundary layer over land. And higher (lower) humidity in the lower (upper) troposphere before than after MCS, indicating signs of upward moisture transported by convection.

During MCS, specific and relative humidity profiles are notably higher than right before and after MCS throughout the troposphere. This implies that events with the highest water vapor in the upper troposphere (e.g., 200–500-mb layer) tend to be associated with MCS. Since MCS tend to produce higher precipitation

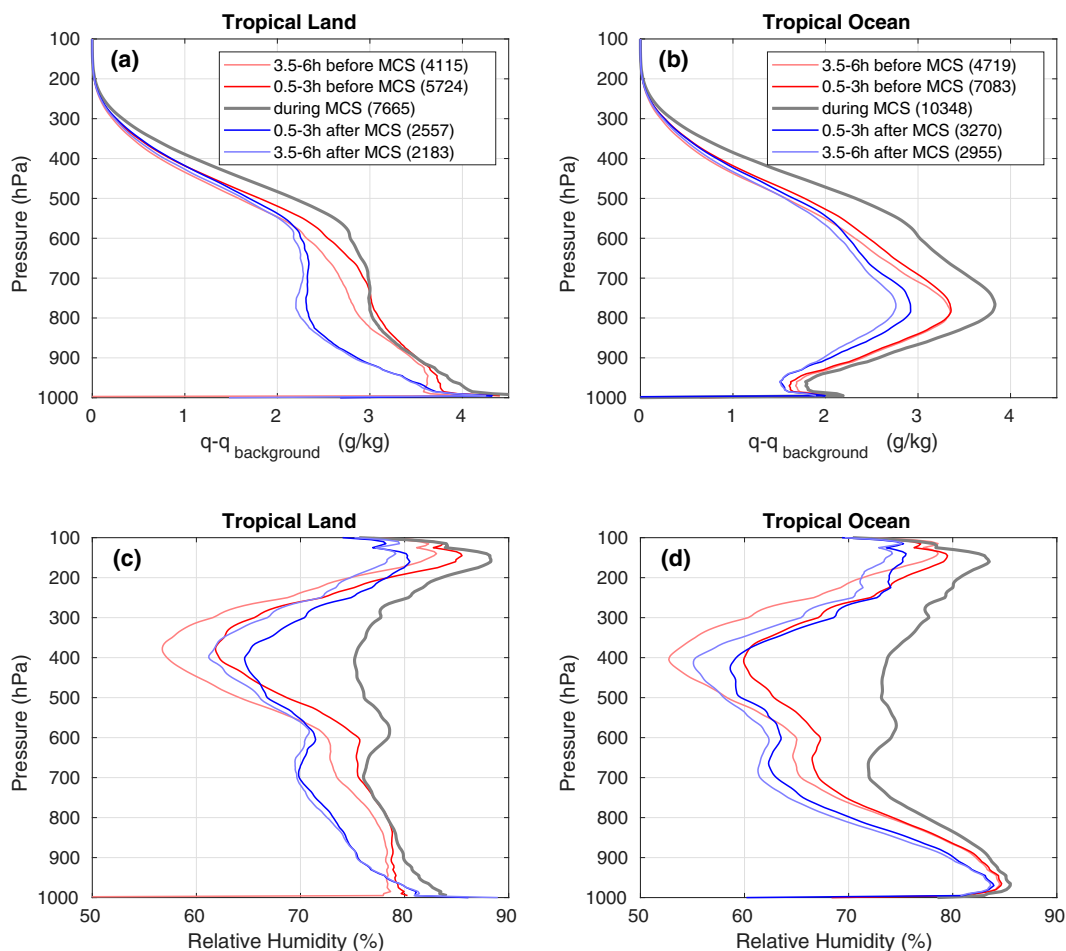


FIG. 9. As in Figs. 7 and 8, but for profiles before (red), during (gray), and after (blue) MCS. (a),(b)  $q_{\text{background}}$  is the average of profiles with no MCS in the  $\pm 12$ -h window of RO observations, and the numbers in the parentheses in the legend indicate number of samples in each case. The standard errors are comparable with the line width chosen used here because of the large sample size. Note that the MCS cases have a greater sample size, associated with the substantial duration of MCS. Also, the before-MCS cases have great sample size than their after-MCS counterparts because RO observations between two consecutive MCS events are classified as before-MCS.

compared with non-MCS cases given the same water vapor value Schiro et al. (2020), this partly explains why the precipitation conditionally averaged on 200–500-mb-layer water vapor in Figs. 2 and 3 also tends to sharply increase with layer water vapor, and why excluding events associated MCS would result in less sensitive dependence of precipitation on 200–500-mb-layer water vapor (not shown).

## 6. Conclusions

This study explores the advantages of assessing precipitation transition statistics using environmental (temperature and moisture) products obtained from GNSS radio occultations (RO). By virtue of their L-band (1.5-GHz) frequency, RO signals are able to directly sense in and near regions of heavy precipitation and clouds. Thermodynamic data spanning between 2006 and 2017 from the COSMIC mission have been used in combination with the global surface precipitation product IMERG in order to

investigate the relationship between precipitation and vertical integrated column water vapor in a global scale. Moreover, the high vertical resolution of RO allowed us to split the troposphere in several regions of interest, not being restricted to the total column.

The precipitation conditionally averaged on layer-integrated water vapor (integrated between different pressure levels within the free troposphere) generally shows a pickup, with precipitation increasing as water vapor increases (Figs. 2 and 3). While true for all the vertical layers and all horizontal regions examined, the precipitation–layer-integrated water vapor relationship has certain interesting features. One is the different behavior of the 850–950-mb layer, representing the lowest part of the free troposphere including part of the boundary layer. The pickup curve for this layer is weaker than for the rest of the vertical layers over land, and much weaker for the ocean cases. This feature reinforces conditional instability calculations at particular radiosonde sites (Holloway and Neelin 2010; Schiro and Neelin 2019) that suggest that the onset of deep convection has a larger



dependence on the free troposphere than on the boundary layer because it has large variations that influence plume buoyancy by entrainment, with dry air tending to prevent onset of deep convection even if a nonentraining plume from the boundary layer would be unstable. Such calculations also suggest that the influence of the boundary layer is larger over land than it is over ocean where variations tend to be small, consistent with findings here over the global tropics.

Another relevant feature is the difference between the different regions of the free troposphere. There is a subtle but important difference between the precipitation–layer-integrated water vapor relationships for the 500–850-mb pressure level (LFT) and for the 200–500-mb level (UFT): in the curve for the 200–500 mb, precipitation smoothly increases even in the lower range of layer-integrated water vapor values, while for the 500–850-mb case, the precipitation sharply increases after a certain value of layer-integrated water vapor. Such behavior is better noticed in Figs. 5 and 6, where the collapse for all the temperature curves is shown. It can be seen how for the 500–850-mb case, precipitation starts to increase for layer-integrated water vapor values close to the critical one (values larger than 0.75) and then increases sharply, whereas for the 200–500-mb case, the precipitation is increasing smoothly at values larger than 0.5. This means that even the definition of a critical value is ambiguous for the upper troposphere, since there is no clear *critical value* after which precipitation sharply increases. This is consistent with the hypothesis that the LFT has a stronger (and causal) influence on the onset of deep convection due to effects of entrainment on buoyancy before a plume reaches the freezing level, while association of high water vapor values and convection in the upper troposphere are substantially due to detrainment.

The dependence on temperature of the pickup curves is well quantified by a critical partial column water vapor value. Specifically, the conditional-average precipitation curves as a function of layer-integrated water vapor collapse to approximately the same dependence, when the layer-integrated water vapor is normalized by a critical value characterizing where the curve picks up for each temperature. When plotted against temperature, these critical values roughly follow a linear increase with increasing temperature (Figs. 4 and 5) for three different pressure layers. These figures also show how the curves nicely collapse when plotted using the critical value fraction.

The  $LWV_{crit}$  for every temperature represents a fraction of the partial column saturation water vapor for the same tropospheric layer and temperature. This fraction is always smaller than the saturation value, and it becomes a smaller fraction as temperature increases. This indicates that the relationship with saturation is more complex than a constant RH value triggering the onset of deep convection. Again, such relationships and hypothesis are clearer over ocean than over land.

In a more detailed investigation of the causal relationships between the water vapor and the precipitation, in Figs. 7–9 we observe how humidity profiles change depending on the time with respect to convection. These figures clearly show that the upper free troposphere is moistened after convection, while the lower troposphere is consistently moistened before and during convection. Similar results hold when considering all instances of precipitation (with an interval of no precipitation

beforehand) or when considering times before, during and after MCS. This implies that the lower troposphere needs to be moist in order to trigger convection, which then can transport moisture upward moistening the upper troposphere.

Overall, this study provides a new set of precipitation transition statistics for different ocean and land regions, with an emphasis on the possibility to separate the contribution of different vertical layers within the free troposphere from the RO observations. Such analysis details the role that the different vertical layers of the free troposphere have in precipitation scenarios. The lower free troposphere plays a causal role in the onset of deep convection, while the upper layers are moistened by convection. These results can potentially be used to give additional insights for constraining convective parameterizations, by comparing model output with these diagnostics to provide a layer by layer view of the relationship of precipitation to its thermodynamic environment. The density of RO sampling is expected to increase substantially in the coming years (Schreiner et al. 2020) permitting methods described here to be refined with soundings that better penetrate into the boundary layer and large tropical datasets.

*Acknowledgments.* Part of this work was performed at the Jet Propulsion Laboratory, California Institute of Technology, under a contract with NASA. R. Padullés research was partially supported by an appointment to the NASA Postdoctoral Program at the Jet Propulsion Laboratory, administered by Universities Space Research Association under contract with NASA. RP has also received funding from the postdoctoral fellowships programme Beatriu de Pinós, funded by the Secretary of Universities and Research (Government of Catalonia) and by the Horizon 2020 programme of research and innovation of the European Union under the Marie Skłodowska-Curie Grant Agreement 801370. The work conducted at the ICE-CSIC was part of the Grant RTI2018-099008-B-C22 funded by the Spanish Ministry of Science and Innovation MCIN/AEI/10.13039/501100011033. The JPL coauthors acknowledge support from the NASA U.S. Participating Investigator (USPI) program. YHK and JDN were supported by National Science Foundation Grant AGS-1936810 and National Oceanic and Atmospheric Administration Grant NA21OAR4310354, and YHK was supported by the JIFRESSE Summer Internship Program (JSIP) during the summer of 2019. The authors thank the three anonymous reviewers for their valuable comments and suggestions that helped improve this article.

*Data availability statement.* COSMIC RO data are available from the UCAR CDAAC, with DOI: 10.5065/ZD80-KD74. IMERG precipitation data are available from GES-DISC, with DOI: 10.5067/GPM/IMERG/3B-HH/06. The merged IR brightness temperature data are available from GES-DISC, with DOI: 10.5067/P4HZB9N27EKU.

## REFERENCES

Ahmed, F., and C. Schumacher, 2017: Geographical differences in the tropical precipitation moisture relationship and rain

- intensity onset. *Geophys. Res. Lett.*, **44**, 1114–1122, <https://doi.org/10.1002/2016GL071980>.
- , and J. D. Neelin, 2018: Reverse engineering the tropical precipitation–buoyancy relationship. *J. Atmos. Sci.*, **75**, 1587–1608, <https://doi.org/10.1175/JAS-D-17-0333.1>.
- , and —, 2019: Explaining scales and statistics of tropical precipitation clusters with a stochastic model. *J. Atmos. Sci.*, **76**, 3063–3087, <https://doi.org/10.1175/JAS-D-18-0368.1>.
- Anthes, R. A., 2011: Exploring Earth’s atmosphere with radio occultation: Contributions to weather, climate and space weather. *Atmos. Meas. Tech.*, **4**, 1077–1103, <https://doi.org/10.5194/amt-4-1077-2011>.
- , and Coauthors, 2008: The COSMIC/FORMOSAT-3 mission: Early results. *Bull. Amer. Meteor. Soc.*, **89**, 313–334, <https://doi.org/10.1175/BAMS-89-3-313>.
- Ao, C. O., 2007: Effect of ducting on radio occultation measurements: An assessment based on high-resolution radiosonde soundings. *Radio Sci.*, **42**, RS2008, <https://doi.org/10.1029/2006RS003485>.
- , T. K. Meehan, G. A. Hajj, and A. J. Mannucci, 2003: Lower troposphere refractivity bias in GPS occultation retrievals. *J. Geophys. Res.*, **108**, 4577, <https://doi.org/10.1029/2002JD003216>.
- , G. A. Hajj, T. K. Meehan, D. Dong, B. A. Iijima, A. J. Mannucci, and E. R. Kursinski, 2009: Rising and setting GPS occultations by use of open-loop tracking. *J. Geophys. Res.*, **114**, D04101, <https://doi.org/10.1029/2008JD010483>.
- Brenowitz, N. D., and C. S. Bretherton, 2018: Prognostic validation of a neural network unified physics parameterization. *Geophys. Res. Lett.*, **45**, 6289–6298, <https://doi.org/10.1029/2018GL078510>.
- Bretherton, C. S., M. E. Peters, and L. E. Back, 2004: Relationships between water vapor path and precipitation over the tropical oceans. *J. Climate*, **17**, 1517–1528, [https://doi.org/10.1175/1520-0442\(2004\)017<1517:RBWVPA>2.0.CO;2](https://doi.org/10.1175/1520-0442(2004)017<1517:RBWVPA>2.0.CO;2).
- Brown, R. G., and C. Zhang, 1997: Variability of midtropospheric moisture and its effect on cloud-top height distribution during TOGA COARE. *J. Atmos. Sci.*, **54**, 2760–2774, [https://doi.org/10.1175/1520-0469\(1997\)054<2760:VOMMAI>2.0.CO;2](https://doi.org/10.1175/1520-0469(1997)054<2760:VOMMAI>2.0.CO;2).
- Chen, D., and Coauthors, 2019: Mesoscale convective systems in the Asian monsoon region from Advanced Himawari Imager: Algorithms and preliminary results. *J. Geophys. Res. Atmos.*, **124**, 2210–2234, <https://doi.org/10.1029/2018JD029707>.
- Cucurull, L., J. C. Derber, R. Treadon, and R. J. Purser, 2007: Assimilation of global positioning system radio occultation observations into NCEP’s Global Data Assimilation System. *Mon. Wea. Rev.*, **135**, 3174–3193, <https://doi.org/10.1175/MWR3461.1>.
- Dee, D. P., and Coauthors, 2011: The ERA-Interim reanalysis: Configuration and performance of the data assimilation system. *Quart. J. Roy. Meteor. Soc.*, **137**, 553–597, <https://doi.org/10.1002/qj.828>.
- de la Torre-Juárez, M., and M. Nilsson, 2003: On the detection of water vapor profiles and thin moisture layers from atmospheric radio occultations. *J. Geophys. Res.*, **108**, 4276, <https://doi.org/10.1029/2002JD002880>.
- Del Genio, A. D., Y. Chen, D. Kim, and M.-S. Yao, 2012: The MJO transition from shallow to deep convection in *CloudSat*/CALIPSO data and GISS GCM simulations. *J. Climate*, **25**, 3755–3770, <https://doi.org/10.1175/JCLI-D-11-00384.1>.
- Derbyshire, S. H., I. Beau, P. Bechtold, J. Y. Grandpeix, J. M. Piriou, J. L. Redelsperger, and P. M. M. Soares, 2004: Sensitivity of moist convection to environmental humidity. *Quart. J. Roy. Meteor. Soc.*, **130**, 3055–3079, <https://doi.org/10.1256/qj.03.130>.
- Elsaesser, G. S., and C. D. Kummerow, 2013: A multisensor observational depiction of the transition from light to heavy rainfall on subdaily time scales. *J. Atmos. Sci.*, **70**, 2309–2324, <https://doi.org/10.1175/JAS-D-12-0210.1>.
- Feng, Z., L. R. Leung, R. A. Houze Jr., S. Hagos, J. Hardin, Q. Yang, B. Han, and J. Fan, 2018: Structure and evolution of mesoscale convective systems: Sensitivity to cloud microphysics in convection-permitting simulations over the United States. *J. Adv. Model. Earth Syst.*, **10**, 1470–1494, <https://doi.org/10.1029/2018MS001305>.
- , R. A. Houze Jr., L. R. Leung, F. Song, J. C. Hardin, J. Wang, W. I. Gustafson, and C. R. Homeyer, 2019: Spatio-temporal characteristics and large-scale environments of mesoscale convective systems east of the Rocky Mountains. *J. Climate*, **32**, 7303–7328, <https://doi.org/10.1175/JCLI-D-19-0137.1>.
- , F. Song, K. Sakaguchi, and L. R. Leung, 2021: Evaluation of mesoscale convective systems in climate simulations: Methodological development and results from MPAS-CAM over the United States. *J. Climate*, **34**, 2611–2633, <https://doi.org/10.1175/JCLI-D-20-0136.1>.
- Fiolleau, T., and R. Roca, 2013: An algorithm for the detection and tracking of tropical mesoscale convective systems using infrared images from geostationary satellite. *IEEE Trans. Geosci. Remote Sens.*, **51**, 4302–4315, <https://doi.org/10.1109/TGRS.2012.2227762>.
- Gentemann, C. L., and Coauthors, 2020: FluxSat: Measuring the ocean–atmosphere turbulent exchange of heat and moisture from space. *Remote Sens.*, **12**, 1796, <https://doi.org/10.3390/rs12111796>.
- Hajj, G. A., E. R. Kursinski, L. J. Romans, W. I. Bertiger, and S. S. Leroy, 2002: A technical description of atmospheric sounding by GPS occultation. *J. Atmos. Sol.-Terr. Phys.*, **64**, 451–469, [https://doi.org/10.1016/S1364-6826\(01\)00114-6](https://doi.org/10.1016/S1364-6826(01)00114-6).
- Healy, S. B., 2001: Radio occultation bending angle and impact parameter errors caused by horizontal refractive index gradients in the troposphere: A simulation study. *J. Geophys. Res.*, **106**, 11 875–11 889, <https://doi.org/10.1029/2001JD900050>.
- , and J. R. Eyre, 2000: Retrieving temperature, water vapour and surface pressure information from refractive index profiles derived by radio occultation: A simulation study. *Quart. J. Roy. Meteor. Soc.*, **126**, 1661–1683, <https://doi.org/10.1256/smsqj.56606>.
- , A. M. Jupp, and C. Marquardt, 2005: Forecast impact experiment with GPS radio occultation measurements. *Geophys. Res. Lett.*, **32**, L03804, <https://doi.org/10.1029/2004GL020806>.
- Hersbach, H., C. Peubey, A. J. Simmons, P. Berrisford, P. Poli, and D. Dee, 2015: ERA-20CM: A twentieth-century atmospheric model ensemble. *Quart. J. Roy. Meteor. Soc.*, **141**, 2350–2375, <https://doi.org/10.1002/qj.2528>.
- Ho, S. P., and Coauthors, 2020a: Initial assessment of the COSMIC-2/FORMOSAT-7 neutral atmosphere data quality in NESDIS/STAR using in situ and satellite data. *Remote Sens.*, **12**, 4099, <https://doi.org/10.3390/rs12244099>.
- , and Coauthors, 2020b: The COSMIC/FORMOSAT-3 radio occultation mission after 12 years: Accomplishments, remaining challenges, and potential impacts of COSMIC-2. *Bull. Amer. Meteor. Soc.*, **101**, E1107–E1136, <https://doi.org/10.1175/BAMS-D-18-0290.1>.

- Holloway, C. E., and J. D. Neelin, 2009: Moisture vertical structure, column water vapor, and tropical deep convection. *J. Atmos. Sci.*, **66**, 1665–1683, <https://doi.org/10.1175/2008JAS2806.1>.
- , and —, 2010: Temporal relations of column water vapor and tropical precipitation. *J. Atmos. Sci.*, **67**, 1091–1105, <https://doi.org/10.1175/2009JAS3284.1>.
- Houze, R. A., Jr., 1993: *Cloud Dynamics*. Academic Press, 573 pp.
- Huffman, G., E. F. Stocker, D. Bolvin, E. Nelkin, and J. Tan, 2019a: GPM IMERG final precipitation L3 half hourly 0.1 degree  $\times$  0.1 degree V06. NASA GES DISC, accessed 9 February 2021, <https://doi.org/10.5067/GPM/IMERG/3B-HH/06>.
- , and Coauthors, 2019b: NASA Global Precipitation Measurement (GPM) Integrated Multi-satellitE Retrievals for GPM (IMERG). NASA Algorithm Theoretical Basis Doc., 38 pp., [https://gpm.nasa.gov/sites/default/files/document\\_files/IMERG\\_ATBD\\_V06.pdf](https://gpm.nasa.gov/sites/default/files/document_files/IMERG_ATBD_V06.pdf).
- Janowiak, J., B. Joyce, and P. Xie, 2017: NCEP/CPC L3 half hourly 4 km global (60S–60N) merged IR V1 (GPM\_MERGIR). NASA GES DISC, accessed 7 January 2020, <https://doi.org/10.5067/P4HZB9N27EKU>.
- Kingsmill, D. E., and R. A. Houze Jr., 1999: Kinematic characteristics of air flowing into and out of precipitating convection over the west Pacific warm pool: An airborne Doppler radar survey. *Quart. J. Roy. Meteor. Soc.*, **125**, 1165–1207, <https://doi.org/10.1002/cj.1999.49712555605>.
- Kuo, Y.-H., W. S. Schreiner, J. K. Wang, D. L. Rossiter, and Y. Zhang, 2005: Comparison of GPS radio occultation soundings with radiosondes. *Geophys. Res. Lett.*, **32**, L05817, <https://doi.org/10.1029/2004GL021443>.
- , C. R. Mechoso, and J. D. Neelin, 2017: Tropical convective onset statistics and causality in the water vapor–precipitation relation. *J. Atmos. Sci.*, **74**, 915–931, <https://doi.org/10.1175/JAS-D-16-0182.1>.
- , J. D. Neelin, and K. A. Schiro, 2018: Convective transition statistics over tropical oceans for climate model diagnostics: Observational baseline. *J. Atmos. Sci.*, **75**, 1553–1570, <https://doi.org/10.1175/JAS-D-17-0287.1>.
- , and Coauthors, 2020: Convective transition statistics over tropical oceans for climate model diagnostics: GCM evaluation. *J. Atmos. Sci.*, **77**, 379–403, <https://doi.org/10.1175/JAS-D-19-0132.1>.
- Kursinski, E. R., G. A. Hajj, J. T. Schofield, R. P. Linfield, and K. R. Hardy, 1997: Observing Earth's atmosphere with radio occultation measurements using the global positioning system. *J. Geophys. Res.*, **102**, 23 429–23 465, <https://doi.org/10.1029/97JD01569>.
- , —, S. Leroy, and B. Herman, 2000: The GPS radio occultation technique. *Terr. Atmos. Ocean. Sci.*, **11**, 53–114, [https://doi.org/10.3319/TAO.2000.11.1.53\(COSMIC\)](https://doi.org/10.3319/TAO.2000.11.1.53(COSMIC)).
- Li, Y., and R. Carbone, 2012: Excitation of rainfall over the tropical western Pacific. *J. Atmos. Sci.*, **69**, 2983–2994, <https://doi.org/10.1175/JAS-D-11-0245.1>.
- Mapes, B. E., 2000: Convective inhibition, subgrid-scale triggering energy, and stratiform instability in a toy tropical wave model. *J. Atmos. Sci.*, **57**, 1515–1535, [https://doi.org/10.1175/1520-0469\(2000\)057<1515:CISSTE>2.0.CO;2](https://doi.org/10.1175/1520-0469(2000)057<1515:CISSTE>2.0.CO;2).
- Mechem, D. B., R. A. Houze Jr., and S. S. Chen, 2002: Layer inflow into precipitating convection over the western tropical Pacific. *Quart. J. Roy. Meteor. Soc.*, **128**, 1997–2030, <https://doi.org/10.1256/003590002320603502>.
- Mohr, K. I., and E. J. Zipser, 1996: Mesoscale convective systems defined by their 85-GHz ice scattering signature: Size and intensity comparison over tropical oceans and continents. *Mon. Wea. Rev.*, **124**, 2417–2437, [https://doi.org/10.1175/1520-0493\(1996\)124<2417:MCSDBT>2.0.CO;2](https://doi.org/10.1175/1520-0493(1996)124<2417:MCSDBT>2.0.CO;2).
- Neelin, J. D., O. Peters, and K. Hales, 2009: The transition to strong convection. *J. Atmos. Sci.*, **66**, 2367–2384, <https://doi.org/10.1175/2009JAS2962.1>.
- Nesbitt, S., W. R. Cifelli, and S. A. Rutledge, 2006: Storm morphology and rainfall characteristics of TRMM precipitation features. *Mon. Wea. Rev.*, **134**, 2702–2721, <https://doi.org/10.1175/MWR3200.1>.
- Núñez Ocasio, K. M. N., J. L. Evans, and G. S. Young, 2020: Tracking mesoscale convective systems that are potential candidates for tropical cyclogenesis. *Mon. Wea. Rev.*, **148**, 655–669, <https://doi.org/10.1175/MWR-D-19-0070.1>.
- Padullés, R., E. Cardellach, K. N. Wang, C. O. Ao, and F. J. Turk, 2018: Assessment of global navigation satellite system (GNSS) radio occultation refractivity under heavy precipitation. *Atmos. Chem. Phys.*, **18**, 11 697–11 708, <https://doi.org/10.5194/acp-18-11697-2018>.
- Parsons, D. B., J. L. Redelsperger, and K. Yoneyama, 2000: The evolution of the tropical western Pacific atmosphere-ocean system following the arrival of a dry intrusion. *Quart. J. Roy. Meteor. Soc.*, **126**, 517–548, <https://doi.org/10.1002/qj.49712656307>.
- Peters, O., and J. D. Neelin, 2006: Critical phenomena in atmospheric precipitation. *Nat. Phys.*, **2**, 393–396, <https://doi.org/10.1038/nphys314>.
- Sahany, S., J. D. Neelin, K. Hales, and R. B. Neale, 2012: Temperature–moisture dependence of the deep convective transition as a constraint on entrainment in climate models. *J. Atmos. Sci.*, **69**, 1340–1358, <https://doi.org/10.1175/JAS-D-11-0164.1>.
- Schiro, K. A., and J. D. Neelin, 2019: Deep convective organization, moisture vertical structure, and convective transition using deep-inflow mixing. *J. Atmos. Sci.*, **76**, 965–987, <https://doi.org/10.1175/JAS-D-18-0122.1>.
- , —, D. K. Adams, and B. R. Lintner, 2016: Deep convection and column water vapor over tropical land versus tropical ocean: A comparison between the Amazon and the tropical western Pacific. *J. Atmos. Sci.*, **73**, 4043–4063, <https://doi.org/10.1175/JAS-D-16-0119.1>.
- , F. Ahmed, S. E. Giangrande, and J. D. Neelin, 2018: GoAmazon2014/5 campaign points to deep-inflow approach to deep convection across scales. *Proc. Natl. Acad. Sci. USA*, **115**, 201719842, <https://doi.org/10.1073/pnas.1719842115>.
- , S. Sullivan, Y.-H. Kuo, H. Su, P. Gentine, G. S. Elsaesser, J. H. Jiang, and J. D. Neelin, 2020: Environmental controls on tropical mesoscale convective system precipitation intensity. *J. Atmos. Sci.*, **77**, 4233–4249, <https://doi.org/10.1175/JAS-D-20-0111.1>.
- Schreiner, W. S., and Coauthors, 2020: COSMIC-2 radio occultation constellation: First results. *Geophys. Res. Lett.*, **47**, e2019GL086841, <https://doi.org/10.1029/2019GL086841>.
- Schröder, M., and Coauthors, 2018: The GEWEX water vapor assessment archive of water vapour products from satellite observations and reanalyses. *Earth Syst. Sci. Data*, **10**, 1093–1117, <https://doi.org/10.5194/essd-10-1093-2018>.
- Sherwood, S. C., S. Bony, and J. L. Dufresne, 2014: Spread in model climate sensitivity traced to atmospheric convective mixing. *Nature*, **505**, 37–42, <https://doi.org/10.1038/nature12829>.
- Sokolovskiy, S. V., 2003: Effect of superrefraction on inversions of radio occultation signals in the lower troposphere. *Radio Sci.*, **38**, 1058, <https://doi.org/10.1029/2002RS002728>.
- Sun, B., A. Reale, D. J. Seidel, and D. C. Hunt, 2010: Comparing radiosonde and COSMIC atmospheric profile data to quantify

- differences among radiosonde types and the effects of imperfect collocation on comparison statistics. *J. Geophys. Res.*, **115**, D23104, <https://doi.org/10.1029/2010JD014457>.
- Tan, J., W. A. Petersen, P. E. Kirstetter, and Y. Tian, 2017: Performance of IMERG as a function of spatiotemporal scale. *J. Hydrometeorol.*, **18**, 307–319, <https://doi.org/10.1175/JHM-D-16-0174.1>.
- , G. J. Huffman, D. T. Bolvin, and E. J. Nelkin, 2019a: Diurnal cycle of IMERG V06 precipitation. *Geophys. Res. Lett.*, **46**, 13 584–13 592, <https://doi.org/10.1029/2019GL085395>.
- , —, —, and —, 2019b: IMERG V06: Changes to the morphing algorithm. *J. Atmos. Oceanic Technol.*, **36**, 2471–2482, <https://doi.org/10.1175/JTECH-D-19-0114.1>.
- Tang, G., M. P. Clark, S. M. Papalexiou, Z. Ma, and Y. Hong, 2020: Have satellite precipitation products improved over last two decades? A comprehensive comparison of GPM IMERG with nine satellite and reanalysis datasets. *Remote Sens. Environ.*, **240**, 111697, <https://doi.org/10.1016/j.rse.2020.111697>.
- Thayer, G. D., 1974: An improved equation for the radio refractive index of air. *Radio Sci.*, **9**, 803–807, <https://doi.org/10.1029/RS009i010p00803>.
- Tompkins, A. M., 2001: Organization of tropical convection in low vertical wind shears: The role of water vapor. *J. Atmos. Sci.*, **58**, 529–545, [https://doi.org/10.1175/1520-0469\(2001\)058<0529:OOTCIL>2.0.CO;2](https://doi.org/10.1175/1520-0469(2001)058<0529:OOTCIL>2.0.CO;2).
- UCAR COSMIC Program, 2006: COSMIC-1 data products (level 2 wetprf dataset). UCAR/NCAR COSMIC, accessed 9 February 2021, <https://doi.org/10.5065/ZD80-KD74>.
- Vergados, P., A. J. Mannucci, and C. O. Ao, 2014: Assessing the performance of GPS radio occultation measurements in retrieving tropospheric humidity in cloudiness: A comparison study with radiosondes, ERA-Interim, and AIRS data sets. *J. Geophys. Res. Atmos.*, **119**, 7718–7731, <https://doi.org/10.1002/2013JD021398>.
- Vila, D. A., L. A. Toledo Machado, H. Laurent, and I. Velasco, 2008: Forecast and Tracking the Evolution of Cloud Clusters (ForTraCC) using satellite infrared imagery: Methodology and validation. *Wea. Forecasting*, **23**, 233–245, <https://doi.org/10.1175/2007WAF2006121.1>.
- Wang, B. R., X. Y. Liu, and J. K. Wang, 2013: Assessment of COSMIC radio occultation retrieval product using global radiosonde data. *Atmos. Meas. Tech.*, **6**, 1073–1083, <https://doi.org/10.5194/amt-6-1073-2013>.
- Yuan, J., and R. A. Houze, 2010: Global variability of mesoscale convective system anvil structure from A-train satellite data. *J. Climate*, **23**, 5864–5888, <https://doi.org/10.1175/2010JCLI3671.1>.
- Zipser, E., 1977: Mesoscale and convective-scale downdrafts as distinct components of squall-line structure. *Mon. Wea. Rev.*, **105**, 1568–1589, [https://doi.org/10.1175/1520-0493\(1977\)105<1568:MACDAD>2.0.CO;2](https://doi.org/10.1175/1520-0493(1977)105<1568:MACDAD>2.0.CO;2).